

Nanoscale phase transitions under extreme conditions within an ion track

Jiaming Zhang, Maik Lang, and Rodney C. Ewing^{a)}

Department of Geological Sciences, University of Michigan, Ann Arbor, Michigan 48109

Ram Devanathan and William J. Weber^{b)}

Pacific Northwest National Laboratory, Richland, Washington 99352

Marcel Toulemonde

Centre Interdisciplinaire de Recherche sur les Ions, les Matériaux et la Photonique (CIMAP), Commissariat à l'énergie atomique et aux énergies alternatives, Centre national de la recherche scientifique, Ecole national supérieure d'Ingénieurs de Caen (CEA-CNRS-ENSICAEN) and University of Caen, 14070 Caen, France

(Received 8 February 2010; accepted 26 April 2010)

The dynamics of track development due to the passage of relativistic heavy ions through solids is a long-standing issue relevant to nuclear materials, age dating of minerals, space exploration, and nanoscale fabrication of novel devices. We have integrated experimental and simulation approaches to investigate nanoscale phase transitions under the extreme conditions created within single tracks of relativistic ions in $\text{Gd}_2\text{O}_3(\text{TiO}_2)_x$ and $\text{Gd}_2\text{Zr}_{2-x}\text{Ti}_x\text{O}_7$. Track size and internal structure depend on energy density deposition, irradiation temperature, and material composition. Based on the inelastic thermal spike model, molecular dynamics simulations follow the time evolution of individual tracks and reveal the phase transition pathways to the concentric track structures observed experimentally. Individual ion tracks have nanoscale core-shell structures that provide a unique record of the phase transition pathways under extreme conditions.

I. INTRODUCTION

Heavy ions traveling at relativistic velocities are created by nuclear fission, high-energy particle accelerators, and cosmic events. Fission-fragment tracks are the primary source of radiation damage in nuclear fuels,¹ and fission tracks in minerals are used extensively for age-dating and thermochronology to reconstruct the time-temperature history of the Earth's crust.^{2,3} Cosmic rays in space can disrupt or damage electronic devices used in space exploration,^{3,4} and ion irradiation is used to create complex nanostructures, such as cylindrical nanopores, nanoscale surface structures, and templates for nanofabrication.^{3,5} The highly localized extreme conditions induced by ions with MeV to GeV energies have been used to manipulate the properties of materials at the nanoscale.^{3,5,6} The resulting nano-sized track is the atomic-scale record of the extreme energy deposition over exceedingly short time periods.

Address all correspondence to these authors.

^{a)}e-mail: rodewing@umich.edu

^{b)}e-mail: wjweber@utk.edu

Present address: University of Tennessee, Knoxville, TN 37996. This author was an editor of this journal during the review and decision stage. For the *JMR* policy on review and publication of manuscripts authored by editors, please refer to http://www.mrs.org/jmr_policy

DOI: 10.1557/JMR.2010.0180

Relativistic heavy ions, often referred to as swift heavy ions, lose their energy predominantly through inelastic interactions with electrons, so-called electronic energy loss, on femtosecond time scales, as shown in Fig. 1. The high density of energy transfer to the electrons along the ion path leads to local states of intense electronic excitation, a confined plasma-like state, that screens the Coulomb field and decreases rapidly away from the center of the track.⁷ Through electron-phonon coupling, the excited electrons transfer their energy to atoms, which are rapidly heated, resulting in local melting and vaporization, with an accompanying pressure wave to the surrounding material.^{7–9} Subsequent melt quenching, recrystallization, and defect recovery occur over nanoscale dimensions during rapid cooling. These collective processes, which occur over pico- to nanosecond time frames (Fig. 1), drive the local atomic structure far from equilibrium, resulting in rapid phase transition pathways through equilibrium and nonequilibrium states that result in the formation of multiple concentric phases within a track that is a few nanometers in diameter and tens of micrometers in length.

The physics of the nonequilibrium phase transitions within a track are similar to those that are caused by ultrashort pulsed laser interactions with solids¹⁰ or structural changes induced by shock waves.¹¹ However, the phase transition pathways accessible within the nanometer size of a track may be different than those accessible

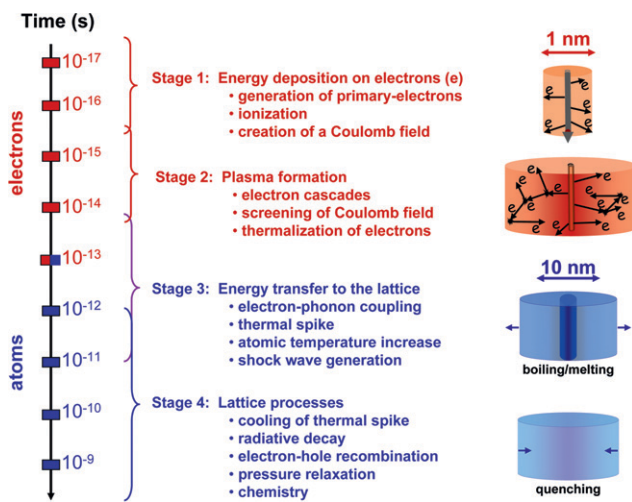


FIG. 1. Schematic illustration of the time evolution of track formation for the series of processes occurring on the nanoscale during the formation of a track due to the passage of a relativistic ion through matter.

during laser or shockwave experiments, and the resulting track provides a record of those pathways. The kinetics of phase transitions in nanoscale materials are greatly affected by pressure,¹² and recent results¹³ have demonstrated the stabilization of metastable phases under relativistic ion irradiation at high pressures. Thus, the study of phase transitions occurring within a single ion track as functions of initial structure type, composition, temperature, and pressure provides a unique opportunity to explore nonequilibrium phase transition pathways in materials to both better understand and model phase transitions under extreme conditions and to search for new structure types with unique properties.

In this study, we show that multiple nanoscale phase transitions occur far from equilibrium under the extreme conditions within individual tracks in $\text{Gd}_2\text{O}_3(\text{TiO}_2)_x$ and $\text{Gd}_2\text{Zr}_{2-x}\text{Ti}_x\text{O}_7$. These and related pyrochlore materials find application as inert matrix fuels for burning actinides,¹⁴ burnable neutron absorber materials to increase nuclear fuel burnup,¹⁵ nuclear waste forms,^{16–19} fast ionic conductors,²⁰ catalysts,²¹ and metallic frustrated magnets.²² Studying phase transitions within single ion tracks in $\text{Gd}_2\text{O}_3(\text{TiO}_2)_x$ and $\text{Gd}_2\text{Zr}_{2-x}\text{Ti}_x\text{O}_7$ as functions of structure type, composition, and temperature provides a unique opportunity to explore nonequilibrium phase transition pathways in this class of materials to better understand and model phase transitions under extreme conditions, and the combined experimental and computational methods demonstrate an approach to search for new structure types with unique properties.

II. MATERIALS AND METHODS

A. Materials

The $\text{Gd}_2\text{O}_3(\text{TiO}_2)_x$ system has a range of stoichiometries, including Gd_2TiO_5 ($x = 1$) and $\text{Gd}_2\text{Ti}_2\text{O}_7$ ($x = 2$).

For Gd_2TiO_5 , there are two polymorphs at low and high temperature: orthorhombic and hexagonal phases, respectively.²³ The orthorhombic Gd_2TiO_5 ($Pnam$, $Z = 4$) is an ordered structure with no mixed-occupancy sites.²⁴ Each Gd cation is seven-coordinated in a polyhedron, while each Ti cation is five-coordinated in a square pyramid. The hexagonal Gd_2TiO_5 ($P6_3/mmc$, $Z = 12$) is a disordered close packed structure with six layers: ABABAB. The octahedral sites on the 6_3 axis between the first and second and between the fourth and fifth layers are entirely occupied by the Gd cations. The mixed cation site is located on the threefold axis at the levels of the third and sixth layers between two neighboring tetrahedral sites in the hexagonal close packing, so that the cation coordination polyhedron is a trigonal bipyramidal. The mixed site is 80% occupied by Gd or Ti cations in the tetrahedral sites, and the vacancies provide a charge compensation mechanism.²⁴

The $\text{A}_2\text{B}_2\text{O}_7$ stoichiometry, including the $\text{Gd}_2\text{Zr}_{2-x}\text{Ti}_x\text{O}_2$ binary, has an isometric, ordered pyrochlore structure ($Fd\bar{3}m$) as a derivative of the ideal fluorite structure, AX_2 ($Fm\bar{3}m$) with cations ordered on the A site and B site and one-eighth of the anions absent.^{25,26} The anion “vacancies” are ordered on the anion sublattice. The A-site cation is eight-coordinated and located within a distorted cubic coordination polyhedron; whereas, the B-site cation is six-coordinated and located within a distorted octahedron. By changing the composition in the $\text{A}_2\text{B}_2\text{O}_7$ stoichiometry (decrease of cation radius ratio r_A/r_B), the ordered pyrochlore can be transformed to a disordered, defect fluorite structure ($Fm\bar{3}m$), for which the A- and B-type cations are randomly distributed over the A sites and B sites, and the oxygen vacancies are disordered on the anion sublattice. In addition to this compositionally driven transformation,¹⁹ the disordered, defect fluorite structure is also induced at elevated temperatures and pressures.^{27,28} Finally, ion beam studies have shown that disordering to the fluorite phase can also be obtained by irradiation,^{16,29–31} but the specific response of the pyrochlore structure depends strongly on chemical composition.

The polycrystalline samples with composition Gd_2TiO_5 , $\text{Gd}_2\text{Ti}_2\text{O}_7$, $\text{Gd}_2\text{ZrTiO}_7$, and $\text{Gd}_2\text{Zr}_2\text{O}_7$ were prepared by the sol-gel method, followed by a sintering at 1875 K for 50 h in air, as described previously.²⁸ The grain size in these samples was on the order of 2 μm . All the samples were polished down to $\sim 40 \mu\text{m}$ thickness with roughness less than 1 μm for irradiation.

B. Experimental methods

The samples were irradiated with either 1.1 GeV ^{101}Ru or 2.2 GeV ^{197}Au ions using the X0 beam line of the UNILAC linear accelerator at the GSI Helmholtz Center for Heavy Ion Research in Darmstadt, Germany. The irradiation temperature was controlled for several sets of

samples to either 8 or 300 K, and the irradiation flux was limited to $\sim 10^8$ ions/cm²·s to avoid significant sample heating. To be able to image the individual ion tracks, the fluence was limited to $5 \times 10^{10} - 1 \times 10^{11}$ ions/cm². Ion range and energy loss, dE/dx , were calculated with the SRIM 2008 code.³² The energy of both projectiles is sufficient to pass completely through the samples and deposit an almost constant energy per unit path length of ~ 40 keV/nm (gold) and 20 keV/nm (ruthenium). The irradiated samples were prepared for transmission electron microscopy (TEM) by crushing into a fine powder and dispersing onto a holey carbon TEM grid. High-resolution TEM (HRTEM) characterization was performed using a JEOL 2010F (Tokyo, Japan) instrument operating at 200 kV, and tracks imaged by HRTEM were far from any observable grain boundaries. Fast Fourier transform (FFT) analysis of the HRTEM images reveal additional details of the local atomic structure within the ion tracks.

C. Computational methods

The thermal spike-induced formation of tracks in this pyrochlore system was modeled using the molecular dynamics (MD) code DL_POLY3.³³ The atomic interactions are described by the potential consisting of the Buckingham part of the potential of Minervini et al.³⁴ without the shell model. The potential was smoothly joined by a spline function to the Ziegler–Biersack–Littmark potential at close separations to avoid unphysical attraction between ions.³⁵

The simulation cell contained 1,617,000 atoms ($35 \times 35 \times 15$ unit cells) with periodic boundaries. The simulation cell was initially equilibrated at 300 K and zero external pressure in the isothermal-isobaric (NPT) ensemble for 5 ps. The thermal spike simulation was performed in the microcanonical (NVE) ensemble. For comparison, simulations were also performed at constant volume by scaling the velocities of atoms within 0.5 nm from the X and Y boundaries to correspond to a temperature of 300 K. The microstructural evolution was similar under these two simulation conditions. As a result, all the simulations for this study were performed in the microcanonical ensemble. The electronic energy loss of the relativistic ions and subsequent electron-phonon coupling were simulated by an instantaneous deposition of kinetic energy within a cylinder of radius 3 nm running along the entire Z dimension of the box. For simplicity, the energy deposition profile was assumed to be constant across the 3 nm radius, and atoms within the cylinder were given velocities in random direction corresponding to a kinetic energy of 5 eV/atom. Due to density differences, the corresponding electronic energy deposition, dE/dx , was slightly different for the three pyrochlores,

with values of 10, 11, and 12 keV/nm for $\text{Gd}_2\text{Zr}_2\text{O}_7$, Gd_2TiZr_7 , and $\text{Gd}_2\text{Ti}_2\text{O}_7$, respectively. A variable time step algorithm was used and the simulations were run for 50 ps. The atomic trajectories were visualized using VMD software.³⁶

III. RESULTS AND DISCUSSION

A. Track structure

In Gd_2TiO_5 and $\text{Gd}_2\text{Ti}_2\text{O}_7$, individual tracks produced by relativistic ions exhibit concentric zones of crystalline and amorphous domains,²⁹ as shown in Fig. 2, which provide a delicate record of the mechanisms of track formation when imaged in cross-section by HRTEM. In fact, within the extreme environment of individual ion tracks, the entire phase diagram of equilibrium (E) and nonequilibrium (NE) states may be explored (Fig. 2). Maximum energy deposition is at the track center and follows an $\sim 1/r^2$ dependence³⁷ on radial distance, r , that controls radial temperature variations and quenching kinetics.^{38,39} The amorphous track core in Gd_2TiO_5 irradiated with 2.2 GeV Au ions has a diameter of ~ 8 nm [Fig. 2(a)] and represents a quenched molten phase. The cooling rate depends strongly on ambient temperature,³⁸ and rapid quenching within the track core may limit the extent of recrystallization. Within the 3-nm-wide outer concentric shell, the transition to the hexagonal structure [Fig. 2(a)] may be due to epitaxial recrystallization from the melt. FFT analysis of the HRTEM image of the track in Gd_2TiO_5 , as shown in Fig. 3, clearly demonstrates an epitaxial relation between the ordered orthorhombic matrix and disordered hexagonal track shell as $O-(200) // H-(10-2)$ and $O-[010] // H-[211]$.

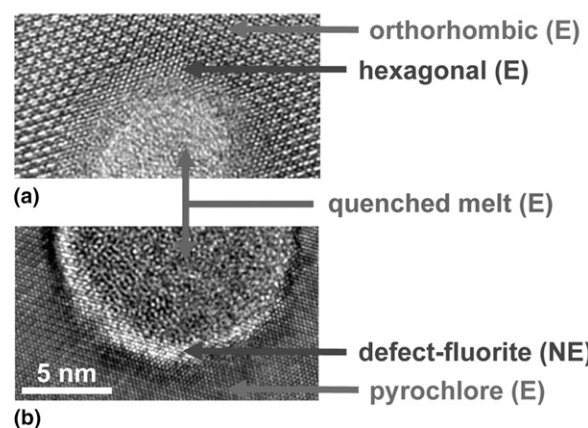


FIG. 2. HRTEM images of 2.2 GeV Au ion tracks and phase relationships in (a) Gd_2TiO_5 and (b) $\text{Gd}_2\text{Ti}_2\text{O}_7$ showing formation of equilibrium (E) and nonequilibrium (NE) phase structures. The highest temperature is at the track center and decreases radially; the corresponding changes in phase with radius map the phase transition pathways in these materials under these extreme conditions and very short timescales.

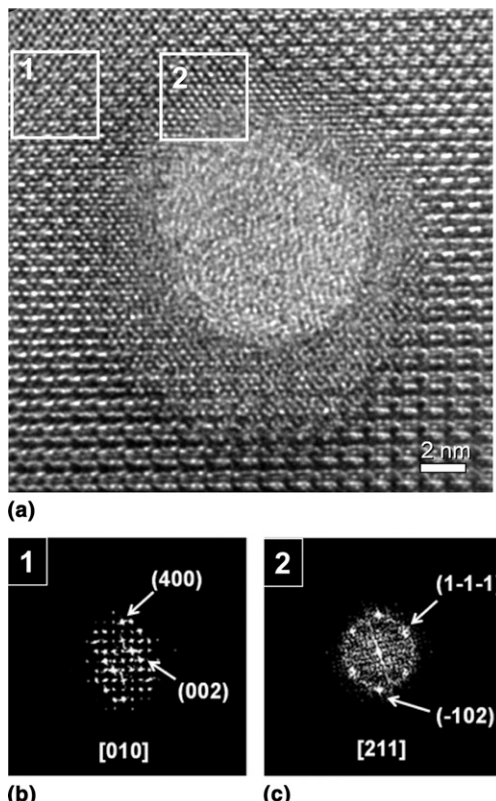


FIG. 3. (a) HRTEM image of the track structure in Gd_2TiO_5 irradiated with 2.2 GeV Au indicating two regions where FFT analyses of the structure were completed. (b) FFT analysis of the structure completely outside the track core/shell (area 1) reveals an orthorhombic structure. (c) FFT analysis of the track shell (area 2) indicates a disordered hexagonal structure that has an epitaxial relationship with the ordered orthorhombic structure.

In the case of $\text{Gd}_2\text{Ti}_2\text{O}_7$, the disordered defect fluorite structure observed within the concentric track shell in Fig. 2(b) is a nonequilibrium phase that is not energetically favored because of the large difference in the radii of the cations.³¹ However, the increased stability of this phase, which has been reported previously,^{29,40} may be due to the nanoscale dimension of the track shell and kinetic limitations for ordering during rapid quenching. The transition zone between the disordered fluorite shell and the ordered pyrochlore matrix shows some strain contrast, which may be associated with a high defect state of pyrochlore. Similar to Gd_2TiO_5 , the track core in $\text{Gd}_2\text{Ti}_2\text{O}_7$ is amorphous due to quenching of a molten state. On the basis of MD simulations described in Sec. III. B, the transformation to the defect-fluorite structure occurs epitaxially at the melt/solid interface during recrystallization, and the extent of the transformation and size of the amorphous core depend on the differences in recrystallization and quench rates.

Because track formation depends on target material, ion mass and energy and external irradiation conditions, a suitable combination of these parameters provides a

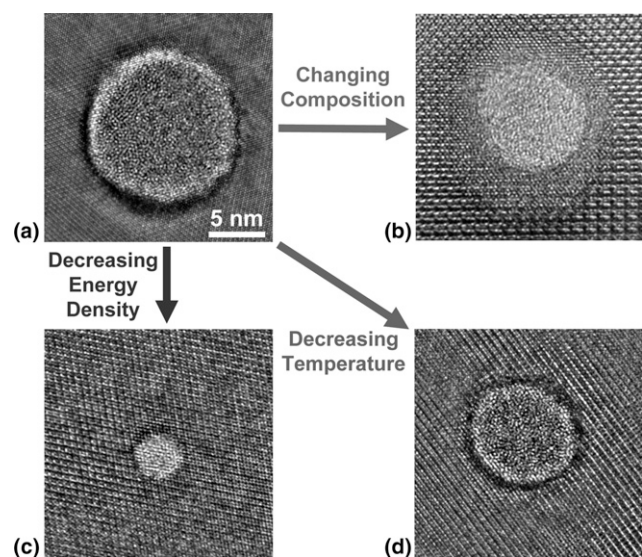


FIG. 4. HRTEM images of ion tracks under changing conditions. (a) Track in $\text{Gd}_2\text{Ti}_2\text{O}_7$ irradiated with 2.2 GeV Au ions (40 keV/nm) at 300 K. (b) Track in Gd_2TiO_5 irradiated with 2.2 GeV Au ions, illustrating the effect of change in composition. (c) Track in $\text{Gd}_2\text{Ti}_2\text{O}_7$ irradiated with 1.1 GeV Ru ions (20 keV/nm) at 300 K, illustrating the effect of a decrease in deposited energy density. (d) Track in $\text{Gd}_2\text{Ti}_2\text{O}_7$ irradiated with 2.2 GeV Au ions (40 keV/nm) at 8 K, illustrating the effect of decreased temperature. The additional effect of high pressure has been demonstrated,¹³ but HRTEM of individual tracks have not been obtained.

means to manipulate track size and morphology (Fig. 4). The crystalline structure of track shells in $\text{Gd}_2\text{O}_3(\text{TiO}_2)_x$ changes from cubic defect fluorite [$x = 2$, Fig. 4(a)] to hexagonal [$x = 1$, Fig. 4(b)], which are disordered polymorphs of the ordered unirradiated material. The change in composition does not significantly affect the overall track size, but the amorphous track core is somewhat smaller and the track shell larger in the case of Gd_2TiO_5 . Compared to the higher deposited energy density (40 keV/nm) in Fig. 4(a), a decrease in deposited energy density (20 keV/nm) in $\text{Gd}_2\text{Ti}_2\text{O}_7$ [Fig. 4(c)] leads to a smaller track size and change in track morphology; however, the disordered shell sizes are similar for the different energy densities, which may indicate the size stability limit for this nonequilibrium structure. Irradiation temperature also influences track size without any apparent change in the core-shell morphology. Tracks produced in $\text{Gd}_2\text{Ti}_2\text{O}_7$ at room temperature (297 K) with 2.2 GeV Au ions [Fig. 4(a)] are slightly larger than tracks formed at 8 K [Fig. 4(d)], which is consistent with the predictions of the inelastic thermal spike model.^{41,42}

Structural variations within single tracks in $\text{Gd}_2\text{Zr}_{2-x}\text{Ti}_x\text{O}_7$ depend strongly on the Zr and Ti content.³¹ For $\text{Gd}_2\text{Ti}_2\text{O}_7$, the amorphous phase is the dominant track structure [Fig. 5(a)]; whereas, for $\text{Gd}_2\text{Zr}_2\text{O}_7$ [Fig. 5(c)], the defect fluorite structure dominates. FFT analysis, as shown in Fig. 6, reveals that the track core in $\text{Gd}_2\text{Zr}_2\text{O}_7$

is converted entirely to the defect fluorite structure without any evidence of amorphous material. The intermediate composition, $\text{Gd}_2\text{ZrTiO}_7$, exhibits both amorphous and defect fluorite domains [Fig. 5(b)], but with a preponderance of the defect fluorite structure as compared with $\text{Gd}_2\text{Ti}_2\text{O}_7$.

B. Simulation of track formation

Realistic simulations of track formation are still somewhat beyond current computational methods, since they must consider energy transfer to electrons, electron transport, electron-phonon coupling, and atomic dynamics. One model for describing phenomena from relativistic heavy ions and predicting track properties is the inelastic thermal spike model,^{41,42} which assumes that a substantial fraction of excited electron energy is absorbed by phonons within a radius defined by the initial electron energy distribution and the electron-phonon coupling mean free path.⁴² This model is easily implemented within an MD simulation environment, as shown in simulations that describe the experimentally observed radial density change within tracks produced in amorphous silica⁴³ and quartz⁴⁴ by relativistic heavy ions.

Large-scale MD dynamic simulations of thermal spikes in $\text{Gd}_2\text{Zr}_{2-x}\text{Ti}_x\text{O}_7$ are used to study track formation dynamics and are compared to the concentric fine structures observed by HRTEM. For $\text{Gd}_2\text{Ti}_2\text{O}_7$ [Fig. 5(d)], the track core is amorphous and surrounded by a defect fluorite structure, with an outermost structure that is highly defective pyrochlore, similar to the

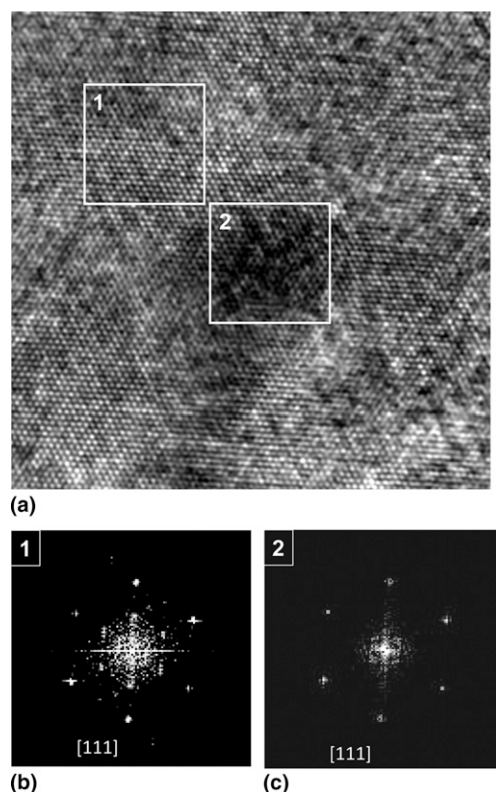


FIG. 6. (a) HRTEM image of the track structure in $\text{Gd}_2\text{Zr}_2\text{O}_7$ irradiated with 2.2 GeV Au at room temperature indicating two regions where FFT analyses of the structure were completed. (b) FFT analysis of the structure outside the track core (area 1) reveals superlattice diffraction maxima consistent with the pyrochlore structure. (c) The disappearance of these superlattice diffraction maxima in the FFT analysis of the track core reveals the defect fluorite structure.

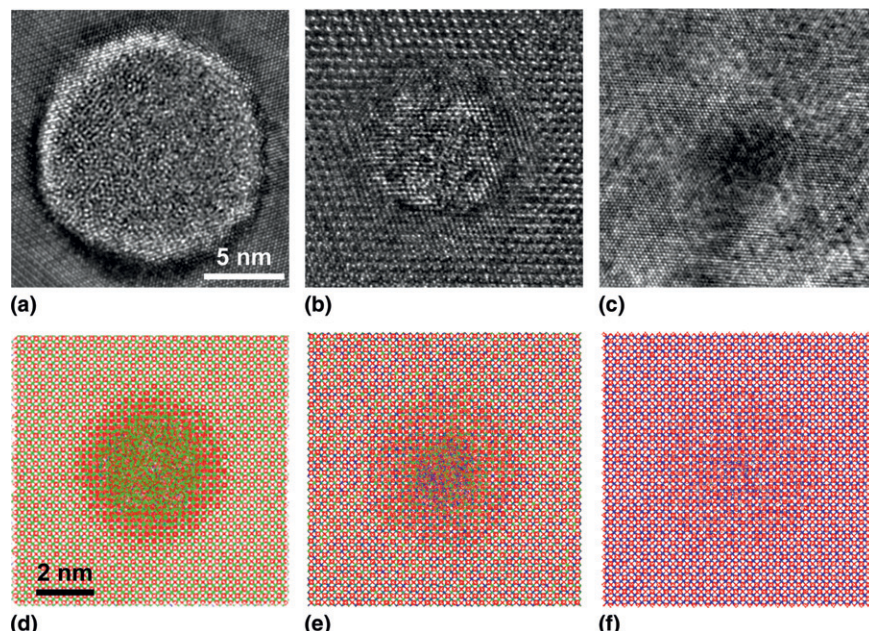


FIG. 5. HRTEM images of the morphology of individual ion tracks produced by 2.2 GeV Au ions (40 keV/nm) in (a) $\text{Gd}_2\text{Ti}_2\text{O}_7$, (b) $\text{Gd}_2\text{TiZrO}_7$, and (c) $\text{Gd}_2\text{Zr}_2\text{O}_7$ are reasonably reproduced by MD thermal spike simulations in (d) $\text{Gd}_2\text{Ti}_2\text{O}_7$ (10 keV/nm), (e) $\text{Gd}_2\text{TiZrO}_7$ (11 keV/nm), and (f) $\text{Gd}_2\text{Zr}_2\text{O}_7$ (12 keV/nm).

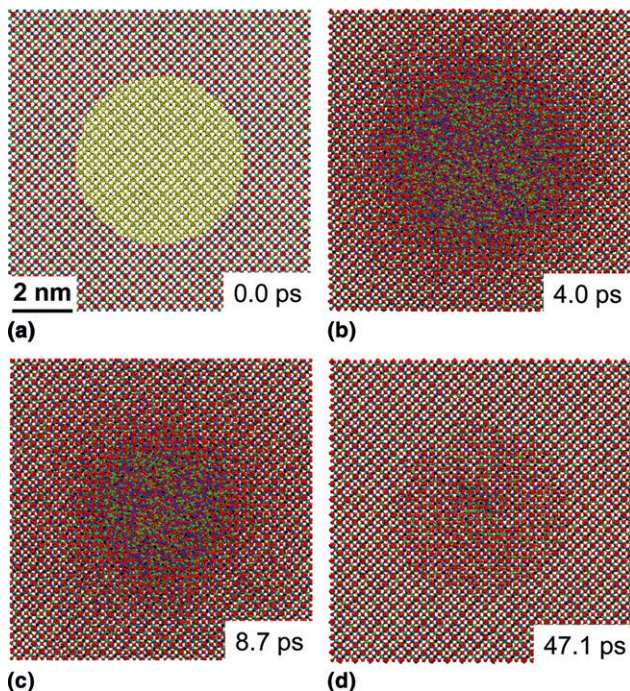


FIG. 7. Molecular dynamics simulations of the time evolution of a thermal spike in $\text{Gd}_2\text{Zr}_2\text{O}_7$: (a) initial energy deposition at $t = 0.0$ ps of 5 eV/atom (12 keV/nm) in the cylindrical zone shown in yellow; (b) after 4.0 ps, the disordered region extends beyond the original melt region; (c) after 8.7 ps, the melt region begins to shrink and recrystallization is evident; and (d) after 47.1 ps, the track has recrystallized to a crystalline defect structure. For all the MD simulations, the oxygen anions are shown in red, while cations are shown in green and blue; only a $10 \text{ nm} \times 10 \text{ nm}$ section of the simulation cell is shown to highlight the structure of the track.

structures observed by HRTEM [Fig. 5(a)] and similar in size to the track in Fig. 4(c), which is at a somewhat comparable energy density when accounting for the efficiency ($\sim 66\%$) of energy deposition within the track by the thermal spike model.⁴² These simulations clearly show the concentric nature of multiple track structures in this class of crystalline materials. For the intermediate composition [Fig. 5(e)], the amorphous core has decreased in radius, and the relative thickness of the defective crystalline shells has increased. In the case of $\text{Gd}_2\text{Zr}_2\text{O}_7$ [Fig. 5(f)], the core does not become amorphous, but has the defect-fluorite structure also observed by HRTEM [Fig. 5(c)]. Track evolution in $\text{Gd}_2\text{Zr}_2\text{O}_7$ with time, as shown in Fig. 7, indicates that the melt state is reached, expands to a radius slightly larger than the initial energy deposition radius, and then contracts fully due to recrystallization, which demonstrates that the final track structure depends on the recrystallization dynamics of the melt state. Similar behavior is observed for $\text{Gd}_2\text{Ti}_2\text{O}_7$, as shown in Fig. 8, except recrystallization is incomplete, and an amorphous core is formed that is smaller than the maximum melt state. These simulations show that track structure depends on complex competition among melting, disordering, and recrystallization

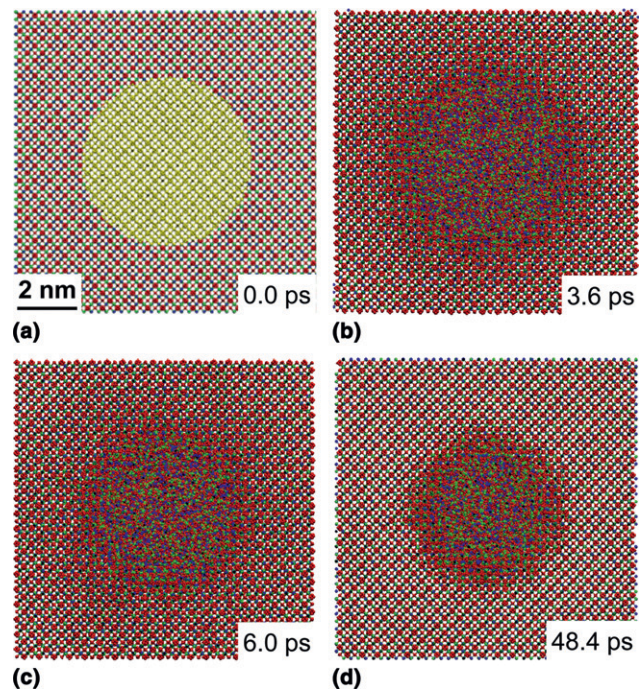


FIG. 8. Molecular dynamics simulations of the time evolution of a thermal spike in $\text{Gd}_2\text{Ti}_2\text{O}_7$. (a) Initial energy deposition at $t = 0.0$ ps of 5 eV/atom (10 keV/nm) in the cylindrical zone shown in yellow. (b) After 3.6 ps, the melt region extends only slightly beyond the original energy deposition zone. (c) After 6.0 ps, the molten core begins to shrink and partial recrystallization is initiated. (d) After 48.4 ps, the final melt-quenched core surrounded by a defective pyrochlore structure. The oxygen anions are shown in red, while cations are in green and blue; only a $10 \text{ nm} \times 10 \text{ nm}$ section of the simulation cell is shown to highlight the structure of the track.

processes. With its high melting temperature, $\text{Gd}_2\text{Zr}_2\text{O}_7$ should begin recrystallizing earlier during the thermal quench. The fact that the stable defect-fluorite structure can readily accommodate the atomic disorder that exists within the melt state, due to similar cation radii, also enhances recrystallization. Recrystallization in $\text{Gd}_2\text{Ti}_2\text{O}_7$ occurs at lower temperatures due to a lower melting point. Epitaxial recrystallization of the disordered defect fluorite state from the melt is observed, but growth of this nonequilibrium phase may be limited thermodynamically as well as kinetically. Furthermore, the ionic conductivity arising from oxygen ion transport in $\text{Gd}_2\text{Zr}_2\text{O}_7$ is four orders of magnitude higher²⁰ than that of $\text{Gd}_2\text{Ti}_2\text{O}_7$. Rapid anion migration in $\text{Gd}_2\text{Zr}_2\text{O}_7$, combined with the presence of oxygen structural vacancies in the pyrochlore and defect fluorite structures, should contribute to rapid dynamic damage recovery as demonstrated recently in yttria-stabilized zirconia.⁴⁵

IV. CONCLUSIONS

These combined experimental and computational results demonstrate that within the extreme environment created by a relativistic heavy ion, nonequilibrium phase

transitions occur within single tracks at a scale of just a few nanometers. The computational model demonstrates how tracks evolve over picoseconds and reveals the importance of recrystallization and defect recovery dynamics on track morphologies, and the final track structures from simulations are in good agreement with HRTEM observations. Together, the experimental results and computational simulations provide the basis for predicting materials response under extreme conditions, searching for new structure types, and exploring nanoscale structural manipulation in related materials used in electrochemical, electronic, and magnetic applications.

ACKNOWLEDGMENTS

This work was primarily supported by the United States Department of Energy (DOE), Office of Basic Energy Sciences under Grant No. DE-FG02-97ER45656 and Contract No. DE-AC05-76RL01830. J.Z. and M.L. were partially supported as part of the Materials Science of Actinides, an Energy Frontier Research Center funded by the United States Department of Energy, Office of Science, Office of Basic Energy Sciences under Award No. DE-SC0001089. M.L. also acknowledges support from the German Science Foundation DFG. The computations were performed using resources at the Environmental Molecular Sciences Laboratory (EMSL), a national scientific user facility sponsored by the DOE's Office of Biological and Environmental Research. The authors gratefully acknowledge the materials research group at GSI, particularly K. Swartz, for their support during the irradiations and the contribution of C. Dufour (CIMAP Laboratory, Caen, France) to the development of the inelastic thermal spike model.

REFERENCES

- H.J. Matzke and M. Kinoshita: Polygonization and high burnup structure in nuclear fuels. *J. Nucl. Mater.* **247**, 108 (1997).
- R.L. Fleischer and P.B. Price: Techniques for geological dating of minerals by chemical etching of fission fragment tracks. *Geochim. Cosmochim. Acta* **28**, 1705 (1964).
- R.L. Fleischer, P.B. Price, and R.M. Walker: *Nuclear Tracks in Solids* (University of California Press, Berkeley, CA, 1975).
- M. Boscherini, O. Adriani, M. Bongi, L. Bonechi, G. Castellini, R. D'Alessandro, A. Gabbanini, M. Grandi, W. Menn, P. Papini, S.B. Ricciarini, M. Simon, P. Spillantini, S. Straulino, F. Taccetti, M. Tesi, and E. Vannuccini: Radiation damage of electronic components in space environment. *Nucl. Instrum. Methods Phys. Res., Sect. A* **514**, 112 (2003).
- R.L. Fleischer: Nuclear tracks and nanostructures, in *Engineering Thin Films and Nanostructures with Ion Beams*, edited by E. Knystautas (CRC, Marcel Dekker, New York, 2005), p. 491.
- J. Lian, L.M. Wang, S.X. Wang, J. Chen, L.A. Boatner, and R.C. Ewing: Nanoscale manipulation of pyrochlore: New nanocomposite ionic conductors. *Phys. Rev. Lett.* **87**, 14901 (2001).
- G. Schiwietz, K. Czerski, M. Roth, F. Staufenbiel, and P.L. Grande: Femtosecond dynamics—Snapshots of the early ion-track evolution. *Nucl. Instrum. Methods Phys. Res., Sect. B* **225**, 4 (2004).
- G. Szemes: General features of latent track formation in magnetic insulators irradiated with swift heavy ions. *Phys. Rev. B* **51**, 8026 (1994).
- D.K. Avasthi, S. Ghosh, S.K. Srivastava, and W. Assmann: Existence of transient temperature spike induced by SHI: Evidence by ion beam analysis. *Nucl. Instrum. Methods Phys. Res., Sect. B* **219–220**, 206 (2004).
- N. Gedik, D.-S. Yang, G. Logvenov, I. Bozovic, and A.H. Zewail: Nonequilibrium phase transitions in cuprates observed by ultrafast electron crystallography. *Science* **316**, 425 (2007).
- B.L. Holian and P.S. Lomdahl: Plasticity induced by shock waves in nonequilibrium molecular-dynamics simulations. *Science* **280**, 2085 (1998).
- A. San-Miguel: Nanomaterials under high pressure. *Chem. Soc. Rev.* **35**, 876 (2006).
- M. Lang, F. Zhang, J. Zhang, J. Wang, B. Schuster, C. Trautmann, R. Neumann, U. Becker, and R.C. Ewing: Nanoscale manipulation of the properties of solids at high pressure with relativistic heavy ions. *Nat. Mater.* **8**, 793 (2009).
- S. Lutique, D. Staicu, R.J.M. Konings, V.V. Rondinella, J. Somers, and T. Wiss: Zirconate pyrochlore as a transmutation target: Thermal behaviour and radiation resistance against fission fragment impact. *J. Nucl. Mater.* **319**, 59 (2003).
- H.S. Kim, C.Y. Joung, B.H. Lee, S.H. Kim, and D.S. Sohn: Characteristics of $Gd_xM_yO_2$ ($M = Ti, Zr$ or Al) as a burnable absorber. *J. Nucl. Mater.* **372**, 340 (2008).
- S.X. Wang, B.D. Begg, L.M. Wang, R.C. Ewing, W.J. Weber, and K.V. Govidan Kutty: Radiation stability of gadolinium zirconate: A waste form for plutonium disposition. *J. Mater. Res.* **14**, 4470 (1999).
- K.E. Sickafus, L. Minervini, R.W. Grimes, J.A. Valdez, M. Ishimaru, F. Li, K.J. McClellan, and T. Hartmann: Radiation tolerance of complex oxides. *Science* **289**, 748 (2000).
- W.J. Weber and R.C. Ewing: Plutonium immobilization and radiation effects. *Science* **289**, 2051 (2000).
- R.C. Ewing, W.J. Weber, and J. Lian: Nuclear waste disposal—Pyrochlore ($A_2B_2O_7$): A nuclear waste form for the immobilization of plutonium and the “minor” actinides. *J. Appl. Phys.* **95**, 5949 (2004).
- H.L. Tuller: Mixed ionic-electronic conduction in a number of fluorite and pyrochlore compounds. *Solid State Ionics* **52**, 135 (1992).
- R.H. Jones, A.T. Ashcroft, D. Waller, A.K. Cheetham, and J.M. Thomas: Catalytic conversion of methane to synthesis gas over europium iridate, $Eu_2Ir_2O_7$: An in situ study by x-ray diffraction and mass spectroscopy. *Catal. Lett.* **8**, 169 (1991).
- Y. Machida and S. Nakatsuji, S. Onoda, T. Tayama, and T. Sakakibara: Time-reversal symmetry breaking and spontaneous Hall effect without magnetic order. *Nature* **463**, 210 (2010).
- J.L. Waring and S.J. Schneider: Phase equilibrium relationships in the system $Gd_2O_3-TiO_2$. *J. Res. Natl. Bur. Stand. Sec. A* **69**, 255 (1965).
- Yu.F. Shepelev and M.A. Petrova: Crystal structures of Ln_2TiO_5 ($Ln = Gd, Dy$) polymorphs. *Inorg. Mater.* **44**, 1354 (2008).
- M.A. Subramanian, G. Aravamudan, and G.V. Subba Rao: Oxide pyrochlores—A review. *Prog. Solid State Chem.* **15**, 55 (1983).
- B.C. Chakoumakos: Systematics of the pyrochlore structure type, ideal $A_2B_2X_6Y$. *J. Solid State Chem.* **53**, 120 (1984).
- B.J. Wuensch, K.W. Eberman, C. Heremans, E.M. Ku, P. Onnerud, E.M.E. Yeo, S.M. Haile, J.K. Stalick, and J.D. Jorgensen:

- Connection between oxygen-ion conductivity of pyrochlore fuel-cell materials and structural change with composition and temperature. *Solid State Ionics* **129**, 111 (2000).
28. F.X. Zhang, J.W. Wang, J. Lian, M.K. Lang, U. Becker, and R.C. Ewing: Phase stability and pressure dependence of defect formation in $\text{Gd}_2\text{Ti}_2\text{O}_7$ and $\text{Gd}_2\text{Zr}_2\text{O}_7$ pyrochlores. *Phys. Rev. Lett.* **100**, 045503 (2008).
 29. M. Lang, J. Lian, J. Zhang, F. Zhang, W.J. Weber, C. Trautmann, and R.C. Ewing: Single-ion tracks in $\text{Gd}_2\text{Zr}_{2-x}\text{Ti}_x\text{O}_7$ pyrochlores irradiated with swift heavy ions. *Phys. Rev. B* **79**, 224105 (2009).
 30. B.D. Begg, N.J. Hess, D.E. McCready, S. Thevuthasan, and W.J. Weber: Heavy-ion irradiation effects in $\text{Gd}_2(\text{Zr}_x\text{Ti}_{1-x})_2\text{O}_7$ pyrochlores. *J. Nucl. Mater.* **289**, 188 (2001).
 31. J. Lian, L. Wang, J. Chen, K. Sun, R.C. Ewing, J.M. Farmer, and L.A. Boatner: The order-disorder transition in ion-irradiated pyrochlore. *Acta Mater.* **51**, 1493 (2003).
 32. SRIM: (2008, <http://www.srim.org/SRIM/SRIM2008.htm>).
 33. I.T. Todorov, W. Smith, K. Trachenko, and M.T. Dove: DL_POLY_3: New dimensions in molecular dynamics simulations via massive parallelism. *J. Mater. Chem.* **16**, 1911 (2006).
 34. L. Minervini, R.W. Grimes, and K.E. Sickafus: Disorder in pyrochlore oxides. *J. Am. Ceram. Soc.* **83**, 1873 (2000).
 35. J.F. Ziegler, J.P. Biersack, and U. Littmark: *The Stopping and Range of Ions in Matter* (Pergamon Press, New York, 1985).
 36. W. Humphrey, A. Dalke, and K. Schulten: VMD: Visual molecular dynamics. *J. Mol. Graphics* **14**, 33 (1996).
 37. R. Katz, K.S. Loh, L. Baling, and G-R. Huang: An analytical representation of the radial distribution of dose from energetic heavy ions in water, Si, LiF, NaI, and SiO_2 . *Radiat. Eff. Defects Solids* **114**, 15 (1990).
 38. M. Toulemonde, Ch. Dufour, A. Meftah, and E. Paumier: Transient thermal processes in heavy ion irradiation of crystalline inorganic insulators. *Nucl. Instrum. Methods Phys. Res., Sect. B* **166–167**, 903 (2000).
 39. A. Meftah, J.M. Costantini, N. Khalfaoui, S. Boudjadar, J.P. Stoquert, F. Studer, and M. Toulemonde: Experimental determination of track cross-section in $\text{Gd}_3\text{Ga}_5\text{O}_{12}$ and comparison to the inelastic thermal spike model applied to several materials. *Nucl. Instrum. Methods Phys. Res., Sect. B* **237**, 563 (2005).
 40. M. Lang, F.X. Zhang, R.C. Ewing, J. Lian, C. Trautmann, and Z. Wang: Structural modifications of $\text{Gd}_2\text{Zr}_{2-x}\text{Ti}_x\text{O}_7$ pyrochlore induced by swift heavy ions: Disordering and amorphization. *J. Mater. Res.* **24**, 1322 (2009).
 41. M. Toulemonde, C. Dufour, and E. Paumier: Transient thermal process after a high-energy heavy-ion irradiation of amorphous metals and semiconductors. *Phys. Rev. B* **46**, 14362 (1992).
 42. M. Toulemonde, W. Assmann, C. Dufour, A. Meftah, F. Suder, and C. Trautmann: Experimental phenomena and thermal spike model description of ion tracks in amorphisable inorganic insulators. *Mat. Fys. Medd. K. Dan. Vidensk. Selsk.* **52**, 263 (2006).
 43. P. Kluth, C.S. Schnohr, O.H. Pakarinen, F. Djurabekova, D.J. Sprouster, R. Giulian, M.C. Ridgway, A.P. Byrne, C. Trautmann, D.J. Cookson, K. Nordlund, and M. Toulemonde: Fine structure in swift heavy ion tracks in amorphous SiO_2 . *Phys. Rev. Lett.* **101**, 175503 (2008).
 44. O.H. Pakarinen, F. Djurabekova, K. Nordlund, P. Kluth, and M.C. Ridgway: Molecular dynamics simulations of the structure of latent tracks in quartz and amorphous SiO_2 . *Nucl. Instrum. Methods Phys. Res., Sect. B* **267**, 1456 (2009).
 45. R. Devanathan and W.J. Weber: Dynamic annealing of defects in irradiated zirconia-based ceramics. *J. Mater. Res.* **23**, 593 (2008).